THE ASTROPHYSICAL JOURNAL, 367:575–592, 1991 February 1

ACCRETION POWERED PULSARS: CONTINUUM SPECTRA AND LIGHT CURVES OF SETTLING ACCRETION MOUNDS

DAVID J. BURNARD
Physics Department, University of California at Berkeley, Lawrence Livermore National Laboratory, and Apple Computer, Inc.
JONATHAN ARONS
Astronomy and Physics Departments, University of California at Berkeley, and Institute of Geophysics and Planetary Physics, Lawrence Livermore National Laboratory
AND
RICHARD I. KLEIN
Institute for Geophysics and Planetary Physics, Lawrence Livermore National Laboratory, and Astronomy Department, University of California at Berkeley
Received 1989 September 29; accepted 1990 July 30

ABSTRACT

We apply the radiative transfer technique described in Burnard, Klein, and Arons to model the polarimetric spectra expected from a mound of accreting plasma settling subsonically onto the polar cap regions of an X-ray pulsar. We employ an analytical model of the accretion flow near the polar caps of the neutron stars, described briefly here, and demonstrate how the emission from such an accretion mound can be computed from a series of one-dimensional slabs of nonuniform material. We compare the results of our detailed calculations for these slabs with those obtained from a simple mode-coupled modified blackbody model.

We find that the geometry of the elevated mound forces the observer to receive photons from patches whose surfaces subtend a wide range of angles to the line of sight. The resulting averaging of intensity over the surface of the mound greatly reduces the variation in intensity and polarization found in single-slab models. We conclude that single-slab models are inadequate for representing the emission region of all but the lowest luminosity X-ray pulsars; a self-consistent model of both the accretion flow and the radiation field is required.

For the simple mound studied here, in which the mass flux far above the stellar surface is independent of distance from the magnetic axis, the emission from the postshock settling zone does not contain enough low-frequency photons to model the observed spectra of X-ray pulsars, specifically Her X-1. W point out that mound models with steeper gradients and/or additional soft-photon sources are required to explain the large number of low-frequency photons seen in X-ray pulsars. A discussion of the importance of the radiation-dominated shock and its outer sheath (which are neglected in this paper), lead us to suggest that past success achieved using thin uniform backlit slabs can be interpreted dynamically as the Comptonizing layer formed by the shock itself, backlit by the saturated spectrum radiated from mounds of the type described here.

Subject headings: pulsars — radiative transfer — stars: accretion — stars: neutron — X-rays: binaries

I. INTRODUCTION

In the nearly two decades since the discovery of accretion-powered pulsars in binary systems undergoing mass transfer (Giacconi *et al.* 1971), detailed observations of rotation phase-resolved X-ray spectra have revealed a wide variety of emission phenomena.

The accepted view is that the origin of the X-ray emission is the energy derived from accretion from a larger companion star onto a rotating, magnetized neutron star. The pulsations in the X-ray emission are then due to the rotation of the neutron star and the consequent changes of the orientation between the small polar emission regions and the line of sight of the observer. The quasi-exponential roll-offs observed in the spectra at high energy (typically ~ 20 keV, White *et al.* 1983) are consistent with the emission from a hot plasma with a thermal distribution of electrons. Line features in the observed emission from two X-ray pulsars (Trümper *et al.* 1978; Wheaton *et al.* 1979) are thought to be cyclotron line features, corresponding to a magnetic field strength greater than 10^{12} G.

However, to date a quantitative model worthy of the complex X-ray spectra of the objects has yet to emerge. The spectra cannot be fit with any sort of single-temperature model. Most pulsars have much more radiative entropy (i.e., too many low-frequency photons) than is contained in the simple models used in standard analyses of observational data. The greatest successes in spectral interpretation have come with the use of geometrically simple models in which a low-frequency photon source undergoes unsaturated Comptonization in an overlying layer of modest Thomson optical depth (Mészáros and Nagel 1985*a*, *b*). As we will discuss, this model is not directly consistent with simple *dynamical* considerations.

Furthermore, the pulse shapes of the known X-ray pulsars are unique, and often complex functions of both phase and frequency (White *et al.* 1983). This spectral variation as a function of rotation phase, known as the "beaming pattern," is thought to be determined by the geometry and physical conditions of the emission region. Much of the complexity might be due to cyclotron absorption in a structured magnetic field at the surface (e.g., Elsner and Lamb 1976). In any case, the polar-

ization of the continuum X-rays offers a probe into the surface strength and structure of the magnetic field (Mészáros *et al.* 1988). So far, only the torques on neutron stars have provided information on the magnetic evolution of these objects. These measure the magnetic field strength in the outer magnetosphere, thus shedding little light on whether the magnetic field has its origin in the crust or in the deeper interior. The interpretation of the polarimetric, rotation-phase resolved X-ray spectra, therefore, offers a unique opportunity to directly investigate the magnetism of neutron stars. The work described in this paper is a step along the way toward such interpretive tools.

Considerable effort has been spent in attempting to convert the observed spectra into a model of the physical conditions in the polar accretion columns. Most of this work has concentrated on the interpretation of the emission from uniform slab or cylindrical models with a predetermined structure (Nagel 1981; Mészáros and Nagel 1985*a*, *b*). While such studies have validated the basic physical model, and suggested the possible geometrical interpretations of the observed data (Her X-1 as a pencil rather than fan beam, for instance), a self-consistent determination of both the radiation properties of the emitting material and the dynamics of the flow has been lacking.

We consider only those sources where the luminosity is sufficient ($L_x > 10^{36}$ ergs s^{-1}) for radiation pressure to create a strong deceleration of the infalling plasma. The details of the dynamical model are presented elsewhere (Arons and Klein 1990, in preparation).

These models have a cold plasma falling freely along the polar magnetic field which is halted *above* the surface by a shock wave mediated by radiation conduction in a scattering medium. The thermalization optical depth within the shock is much less than unity—the photons scattering through the shock from the subsonically settling plasma below. In the simplest case, where the accreting mass flux is uniform across the polar cap, the postshock emission region assumes a simple mound structure. This settling region is inhomogeneous in both temperature and density with thermalization optical depth in bremsstrahlung much greater than unity. Since the Thompson optical depth of the mound exceeds $\sim\sqrt{m_e c^2/T_e}$, Comptonization of the underlying blackbody can create substantial modifications of the spectrum at higher photon energies. On the other hand, the low-energy photons, created one thermalization optical depth into the mound, can come from differing temperatures, since both the bremsstrahlung and the magnetic scattering cross sections are nongray. Since the local magnetic field direction varies over the surface of such a mound, geometry must also be taken into account when computing the spectra seen by an earthbound observer.

Once the self-consistent temperature and density distribution for such a model polar cap is known, we can apply a detailed transfer calculation (Burnard, Klein, and Arons 1990, hereafter BKA) to yield the radiation intensity of the mound. We can then simulate the mound's spectrum by summing over the visible portions of the accretion mound, taking into account the unique line of sight to each point on the mound surface, and geometrical transformations necessary to convert from the local mound coordinates to the frame of the observer.

These calculations allow us to test the hypothesis that the emergent spectrum from an X-ray pulsar represents the radiation produced by a settling mound, without the further processing by the shock and upstream cold accretion flow suggested by dynamical models. We will find this subsonic flow model to be lacking in a number of respects, when confronted with observational data. Therefore, we suggest that the transfer of photons through the shearing, compressive flow of the shock wave, where the scattering optical depth is moderate, is the essential ingredient needed to make a successful marriage between models of the dynamics of polar cap accretion and the formation of the emergent spectrum. Such a union requires a substantial extension of the transfer techniques used here. In order to show the limitations of essentially static models of the spectrum formation, we neglect the effect of the radiative shock surrounding the mound on the radiation emitted by the mound. While the shock does not contribute many additional photons, Compton recoil in this medium, which has flow velocity of about one-third to one-half the speed of light, will have a significant effect on the energies of the photons passing through the shock. Modeling of the effect of the shock on the emergent radiation will be considered in a future paper. Our calculations *do* show that the emergent polarized fraction of the radiation may be sensitive to the geometry of the emitting surface, as well as having the sensitivity to the global geometric parameters such as the angle between the magnetic field and the rotation axis found in previous studies (Wang and Welter 1981; Leahy 1990). In order to illustrate this point, we treat the radiation emerging from the mound as if it is directly observable at infinity.

The remainder of this paper is organized as follows. In § II, we briefly describe the analytical model used to simulate the accretion flow near the polar caps of the neutron star, and how the emission from such an accretion mound model can be computed. We also describe the physical characteristics of the particular accretion mound model used throughout the remainder of this paper. In § III, we summarize the technique we have developed to compute the spectra and polarimetry from a slab nonuniform material. We also present the results from several of the slab models used to represent portions of the accretion mound, and compare the results of our detailed calculations with those obtained from a simple modified blackbody model in which mode coupling is taken into account. In § IV, we discuss how the radiation field emitted from the accretion mound is constructed from the individual patch models and what observable features such an accretion mound would possess. These observables include pulse profiles as well as phase-resolved spectra and polarimetry. We find, as have previous investigators, that the polarimetric spectra from a single patch show strong variations as the star rotates. If this variability were realistic, polarimetric observations would be highly sensitive to the geometry of the emission region. Such models have been advocated as the emission from the polar caps of Her X-1, for example, Mészaros and Nagel (1985*a*) and Leahy (1990).

By contrast, the elevated mound supported by radiation pressure forces the observer to receive photons from patches whose surfaces subtend a wide range of angles to the line of sight. The resulting averaging of the polarized fraction substantially reduces the sensitivity of a polarimeter to the emission geometry. We use our results to illustrate this averaging.

We compare and contrast the observable features of the model accretion mound presented here with actual observations of several X-ray pulsars in § V, including a brief discussion of the possible implications of our neglect of the radiation-dominated shock and of the outer sheath of cold freely falling plasma in the accretion column. We suggest that past successes achieved using thin uniform backlit slabs might be interpreted dynamically as the Comptonizing layer formed

by the shock itself, backlit by the saturated spectrum radiated from mounds of the type described here. Our conclusions are summarized in § VI.

II. DYNAMICAL MODEL

In order to study the observed emission from X-ray pulsars, we must begin with a self-consistent model of the structure of the radiating area of accretion column. For this purpose, we employ an analytical model developed by Arons and Klein (1990, in preparation) (see a brief outline in Arons 1987), based on the radiation hydrodynamics of the base of the accretion column. The solution of the analytical model yields mass density, radiation energy density, and velocity throughout the postshock region of the column, assuming axisymmetric steady flow parallel to a star-centered dipole magnetic field onto a circular polar cap of area $\theta_c^2 R_*^2$, where θ_c is the opening angle of the polar cap and R_* is the radius of the neutron star. We also make the additional simplifying assumption that the mass flux is independent of distance from the magnetic axis, out to the sharp edge of the plasma flow. In reality, the nature of the mass flux distribution will be determined at the magnetopause where the infalling material becomes entrained in the magnetic field. Spherical accretion flow tends to produce a more uniform accretion flux (Arons and Lea 1980; Burnard, Lea, and Arons 1983), while accretion disks tend to produce "hollow-cone" accretion flows (e.g., Basko and Sunyaev 1976).

These models describe a family of mounds as a function primarily of the accretion luminosity L_c, measured in units of the "transverse" Eddington luminosity L_1. Here θ_c is the opening angle of the polar cap,

$$L_1 \equiv \theta_c L_{\rm Edd} H_\perp ,$$

where $L_{\rm Edd}$ is the conventional Eddington luminosity and $H_\perp$ is the ratio of the Thomson cross section to the Rosseland averaged scattering cross section for radiation flow across B. The Rosseland averaged opacity appears since the structure of the flow and of the radiation field is determined by the diffusion of radiation across the magnetic field. The magnetic field strength at the surface appears as a parameter in the ratio of the cyclotron energy to the temperature, used in determining $H_\perp$. The expressions we use for $H_\perp$ can be found in Arons, Klein, and Lea (1987). The mound solution also has a weaker dependence on the radius and mass of the neutron star through an explicit dependence on the free-fall velocity above the mound.

The significance of L_1 is that for accretion luminosities small compared to L_1, the freely falling plasma *above* the mound is optically thin *across* the magnetic field. By contrast, the "effective" Eddington luminosity

$$L_{\rm Edd}^{\rm eff} \equiv \frac{\theta_c^2 L_{\rm Edd} H_\parallel}{4} .$$

describes the luminosity above which the freely falling plasma is optically thick *along* the magnetic field. $H_\parallel$ is the ratio of the Thomson cross section to the Rosseland averaged scattering cross section for radiation flow along B. The quantity $L_{\rm Edd}^{\rm (eff)} = L_{\rm Edd}(A_{\rm cap}/4\pi R_*^2)H_\parallel$ is the equivalent of the standard Eddington limit for accretion onto a pole rather than onto a sphere. Since radiation can escape from the sides of the flow, $L_c > L_{\rm Edd}^{\rm (eff)}$ does not have the significance of a cessation of flow, in contrast to spherical accretion. Approximately 60% of the known accretion powered pulsars satisfy

$$L_c \gg L_{\rm Edd}^{\rm (eff)} \sim 10^{35.5}\left(\frac{\theta_c}{0.1}\right)^2 \frac{M_*}{1\ M_\odot} H_\parallel \ {\rm ergs\ s^{-1}} ,$$

and

$$L_c \gtrsim L_1 \sim 10^{36.5} \frac{\theta_c}{0.1} \frac{M_*}{M_\odot} H_\perp \ {\rm ergs\ s^{-1}} .$$

Since the temperatures and cyclotron energies in the emission regions are comparable, neither $H_\perp$ nor $H_\parallel$ are large compared to unity.

Accretion flows with luminosities of this magnitude yield mounds which are not well represented by a single flat patch on the surface of the neutron star. The peak of the mound sits at a height

$$H_s \approx (L_c/L_{\rm Edd} H_\parallel)R_*$$

above the surface, where a radiation-dominated shock of Thomson optical depth

$$\tau \sim (2\text{–}3)(c/v_{\rm ff}) \sim 4\text{–}9$$

transforms the free-fall into the subsonically settling material of the mound. When $L_c \gtrsim L_1$, the mound is at least as tall as it is wide. This has significant consequences for the nature of the spectrum and especially for the polarimetry of such objects. Figures 1–3 illustrate such a mound sitting on the surface of the neutron star, including the coordinates needed in describing the observer's view of the mound.

The mass density and radiative energy density below the shock are described by (Arons and Klein 1990, in preparation) the mass density

$$\rho = \rho_* \exp\left[-\frac{(r-R_*)}{h}\right] \exp\left\{\left(\frac{L_c}{L_1}\right)^2\left[1-\left(\frac{r_{\perp *}}{r_c}\right)^2\right]\right\}, \quad (1)$$

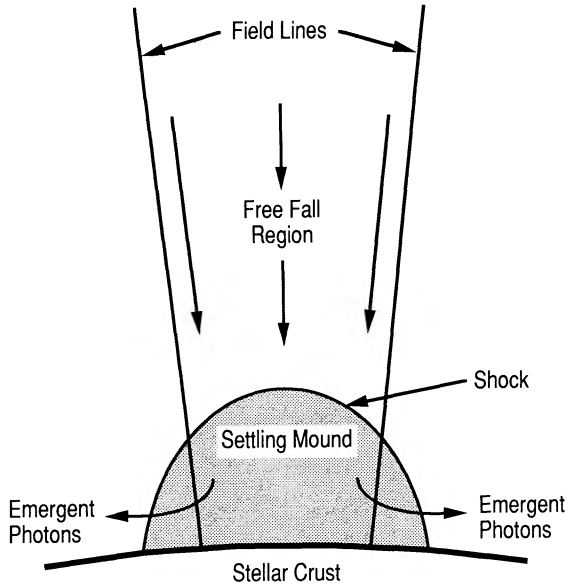

FIG. 1.—Artist's depiction of the accretion flow near the stellar surface showing the infalling material, shock, settling mound material, and emergent radiation.

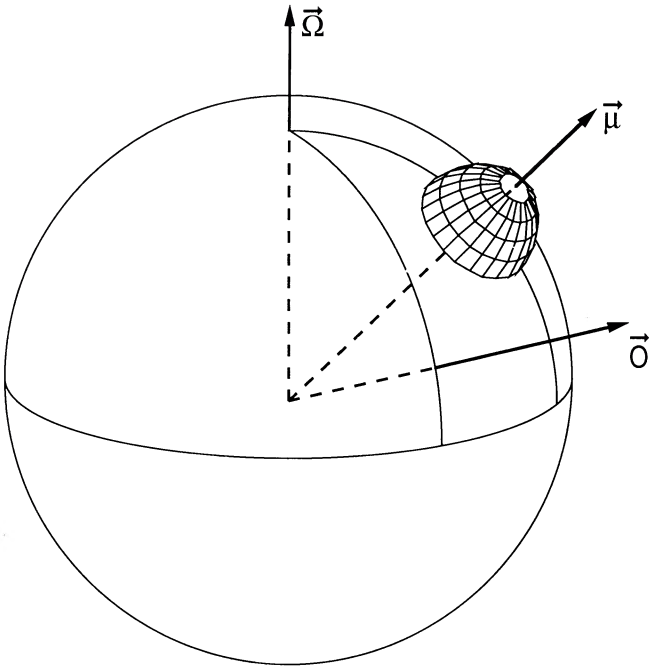

FIG. 2.—Geometry of the polar cap and observer relative to the rotation axis of the neutron star. $\boldsymbol{\Omega}$ is the rotation axis of the star, $\boldsymbol{\mu}$ is the magnetic moment of the star, and $\boldsymbol{O}$ is the direction of the observer.

with

$$\rho_* = 3.7 \times 10^{-3} H_{\|} \left(\frac{M_\odot}{M_* R_{10}^{1/2}}\right)^{1/2} \left(\frac{0.1}{\theta_c}\right)^2 \left(\frac{L_c}{L_1}\right)^2 \frac{\text{g}}{\text{cm}^3},$$

and the radiation pressure

$$p_\gamma = p_* \exp\left[-\frac{4(r - R_*)}{h}\right] \exp\left\{\left(\frac{L_c}{L_1}\right)^2 \left[1 - \left(\frac{r_{\perp *}}{r_c}\right)^2\right]\right\}, \quad (2)$$

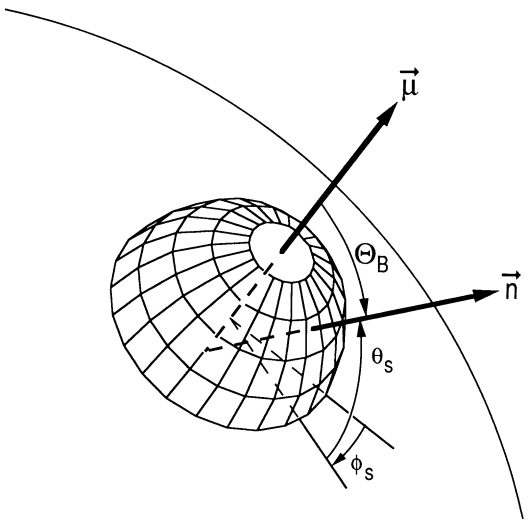

FIG. 3.—Close-up view of the geometry of the accretion mound, $\boldsymbol{\mu}$ is the magnetic moment of the star, which we approximate as the local magnetic field direction $\boldsymbol{B}$. The local slab normal is $\boldsymbol{n}$, and Θ_B is the angle between $\boldsymbol{n}$ and $\boldsymbol{B}$. The angles θ_s and ϕ_s represent the inclination and azimuth of the local slab with respect to the surface of the star at a point corresponding to the central field line.

with

$$p_* = 3 \times 10^{16} \frac{L_c}{10^{37} \text{ ergs s}^{-1}} \left(\frac{10 \text{ km}}{R_*}\right)^{3/2} \left(\frac{1.4\ M_\odot}{M_*}\right)^{1/2} \frac{\text{ergs}}{\text{cm}^3}.$$

Here r is the distance from the star's center, $r_{\perp *}$ is the distance across the cap from the magnetic axis at the base of the accretion column, and $r_c \equiv \theta_c R_*$. The quantities p_* and ρ_* are the radiation pressure and mass density at the outer edge of the mound, where the mound's surface touches the star's crust, while the vertical scale height is

$$h \equiv \frac{L_{\text{Edd}}^{(\text{eff})}}{L_c} R_*.$$

The pressure and density vary across B, increasing at a fixed height by factor of $\exp[(L_c/L_1)^2]$ from the mound's surface to the central field line. The Gaussian scale length of this increase is

$$\Delta r_{\perp *} \equiv \frac{L_1}{L_c} \theta_c R_*.$$

We assume the temperature is given by strict LTE, with $T \propto p_\gamma^{1/4}$. Because the atmospheres are dominated by scattering, this underestimates the true temperature. Improved models for the temperature and their effect on the radiative output will be presented elsewhere. *These models assume the radiation flows almost directly across the magnetic field at the stellar surface itself,* since heat conduction into the star is not important compared to radiation conduction to the edge of the base of the mound. See Arons and Klein (1990, in preparation) for a discussion of this approximation. The models become unrealistic when L_c exceeds $(4\text{–}6)L_1$ because of the exponential dependence of the central density and pressure on $(L_c/L_1)^2$. Nevertheless, their useful range of applicability includes a substantial number of pulsars.

In this paper, we compute the emergent spectrum from the subsonic settling region only. We expect that the X-ray luminosity from the mound L_x will be less than the accretion luminosity, L_c, since, in computing L_x, we neglect photon recoil of mound photons in the shock. In order to see why we should have $L_x < L_c$, consider the energy per gram released as matter falls freely to the top of the shock, $\sim GM_*/(R_* + H_s)$. Above the shock, this is all kinetic energy. Below, the energy released is

$$\frac{GM_*}{R_*}\left(1 - \frac{R_*}{R_* + H_s}\right) \approx \frac{GM_*}{R_*}\frac{H_s}{R_*},$$

with the second form valid when $H_s \ll R_*$. Thus, the energy released by subsonic settling below the shock is smaller than the energy put into the plasma by the shock itself for sub-Eddington luminosities. If the energy released by the shock deceleration is not carried down into the subsonic region, but is *promptly* lost from the plasma by sideways flow of radiation across the magnetic field, the radiative luminosity of the settling flow will be $\sim H_s/R_*$ smaller than L_c itself. Prompt loss of radiation occurs when $L_c \gg L_1$ (Arons and Klein 1990, in preparation). For the model used here, $L_c \gtrsim L_1$. Therefore, we expect and will find that the photon luminosity of our model mound is substantially less than the accretion luminosity, but is still greater than H_s/R_*. The rest of the radiative luminosity from a real pulsar comes from recoil of the mound photons and they pass through the shock, a circumstance which leads us to

a new interpretation of previous radiative transfer results which we discuss in § V.

The input parameters for computing our model are: (1) the accretion luminosity, L_c; (2) the polar cap opening angle, θ_c; (3) the radius and mass of the neutron star; (4) the surface magnetic field strength; and (5) $H_\perp$ and $H_\parallel$. The major dependence on the parameters comes through the combination L_c/L_1. The values characterizing the model column used here are shown in Table 1A. The accretion mound generated from these values is shown in Figure 4. The physical conditions at the surface of the mound are shown in Table 1B.

To solve the transfer equation for the radiation emitted from the accretion mound, we simplify the two-dimensional structure of the surface of the accretion mound shown in Figures 2 and 3 by dividing it into a series of one-dimensional patches. The techniques of representing the details of a two-dimensional photosphere with a series of one-dimensional patches is often used in the study of externally illuminated stellar atmospheres—in the context of X-ray binaries, see, for instance, Anderson (1979), Milgrom and Salpeter (1975), or London and Flannery (1982). Such a technique is applicable if the thermalization optical depth of the mound, and each of the slabs, is large. Our choice of accretion luminosity assures us that the mound has sufficient thermalization optical depth. We are left with the requirement that, in constructing the slabs, we go deep enough into the mound to accumulate a significant thermalization optical depth.

The construction of the one-dimensional patches takes place as follows. We first divide the mound surface into a number of representative regions, as in Figure 4. For this model, whose surface conditions are fairly uniform, we represent the mound with five such regions. In fact, three slabs would be sufficient in this case—one each to represent the three magnetic field orientations present on the mound surface: the top of the mound (slab normal parallel to B), the edge near the surface of the star (slab normal perpendicular to B), and the intermediate region. We then compute equivalent one-dimensional slab models by shooting inward along the normal to the mound surface and calculating the temperature and density along this path from equations (1) and (2) until we accumulate 10–15 thermalization depths.

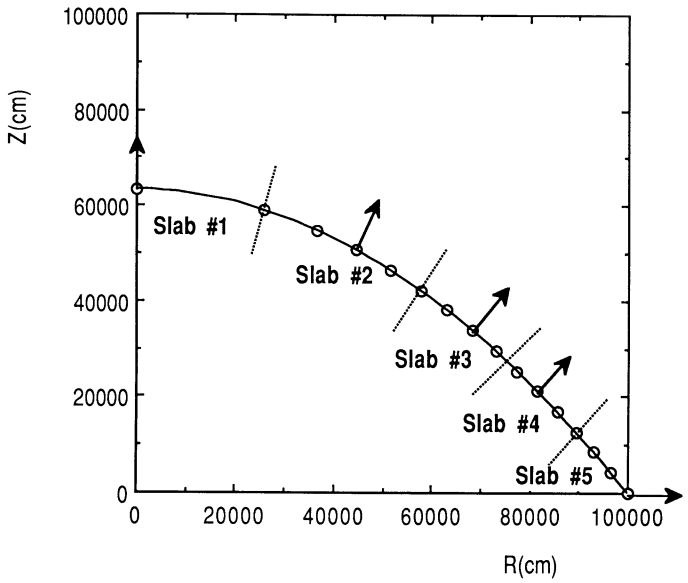

FIG. 4.—Height of the surface of the accretion mound as a function of distance from the center of the pole obtained from the dynamical model of the polar cap. The five regions of the surface to be represented by the five slab models are indicated.

TABLE 1A

MODEL MOUND PARAMETERS

Parameter	Value
Θ_{cap}	0.1 rad
L_c	3E+37
L_1/L_c	0.41
L_1	1.23E+37
L_{Edd}	1.91E+38
R_*	10 km
M_*	1.3 $M_\odot$
B_*	46 keV
$H_\parallel$	2.57
$H_\perp$	1.0

TABLE 1B

SUMMARY OF MOUND SURFACE CONDITIONS

Θ	Height	N_e	T_e	β_{drift}	B
0.0000.....	63230	2.67E+22	7.36	0.0066	38.27
0.0258.....	59020	2.69E+22	7.39	0.0066	38.73
0.0365.....	54810	2.72E+22	7.42	0.0066	39.20
0.0447.....	50600	2.74E+22	7.45	0.0066	39.67
0.0516.....	46390	2.76E+22	7.48	0.0067	40.15
0.0577.....	42180	2.78E+22	7.50	0.0067	40.64
0.0362.....	37970	2.80E+22	7.53	0.0067	41.13
0.0683.....	33750	2.82E+22	7.56	0.0068	41.64
0.0730.....	29540	2.84E+22	7.59	0.0068	42.15
0.0774.....	25330	2.86E+22	7.62	0.0068	42.67
0.0816.....	21120	2.88E+22	7.65	0.0069	43.20
0.0856.....	16910	2.90E+22	7.68	0.0069	43.74
0.0894.....	12700	2.92E+22	7.71	0.0070	44.29
0.0931.....	8486	2.94E+22	7.74	0.0070	44.85
0.0966.....	4275	2.96E+22	7.77	0.0071	45.42
0.0999.....	63	2.98E+22	7.80	0.0071	45.99
0.1000.....	0	2.98E+22	7.80	0.0071	46.00

The outermost region, on the base of the mound, is treated somewhat specially. Simply orienting the slab parallel to the formal surface of the mound is incorrect, since at the mound's base, the radiation flux is directly across B, as mentioned above. Therefore, for this region, we orient the slab so that its normal is perpendicular to B, with the local magnetic field direction for this region set equal to 90°, since the slab surface is now essentially parallel to the local magnetic field. The temperature, density, and Thomson depth profiles for the five slabs are shown in Figures 5–7.

Note that each of the one-dimensional slabs actually represents the conditions for an annular region on the mound. Thus when we compute the total radiation emitted from the mound, we further divide each of the annular regions into a number of identical slab models placed at different orientations around the annulus to simulate the actual mound surface seen by an observer. We found that at least 16 such slabs were required to accurately represent one of these annular regions.

Table 2 summarizes the physical characteristics of the five slab models used to represent the accretion mound. In constructing these slabs we have made several simplifying assumptions. We first assume that the magnetic field is of a uniform strength, with cyclotron frequency $\nu_{cyc} = 44$ keV throughout the mound, whereas the actual variation was from

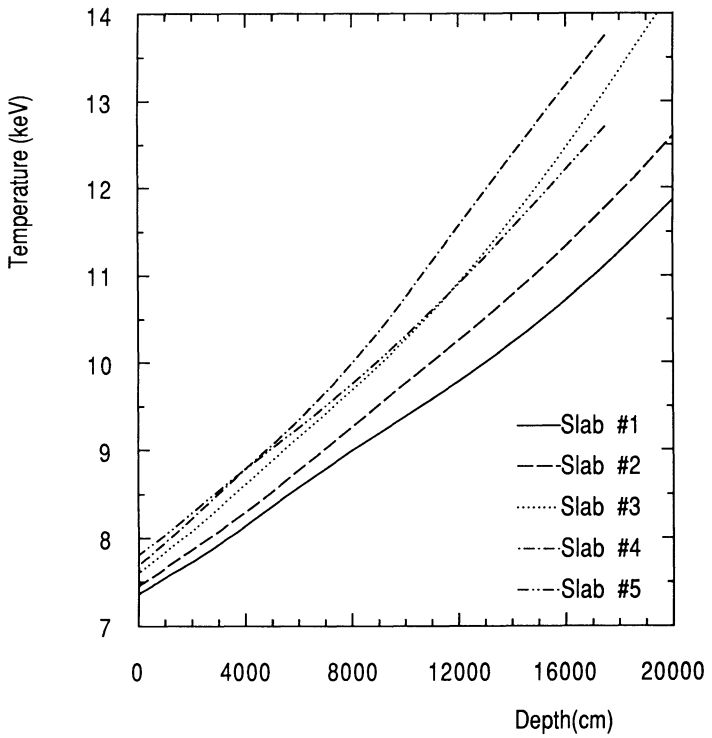

FIG. 5.—Gas temperature as a function of distance into the one-dimensional slabs used in this paper.

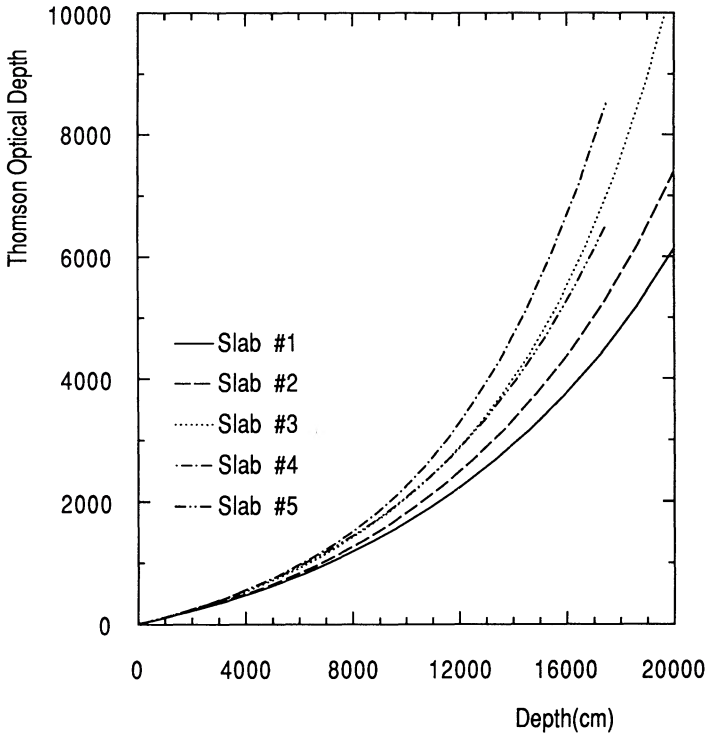

FIG. 7.—Thomson optical depth as a function of distance into the one-dimensional slabs used in this paper.

46 keV at the surface of the star down to 38 keV at the central peak of the mound. This approximation is adequate because of the way we treat the cyclotron line, discussed below.

We also assume that the downward drift velocity of the postshock material in the mound can be neglected. As can be seen from Table 1B, the actual drift velocity is nonrelativistic, with $v/c \sim 1\%$. The effect of this small drift velocity would be to introduce a small forward-backward asymmetry into the scattering cross section with respect to the magnetic field direction.

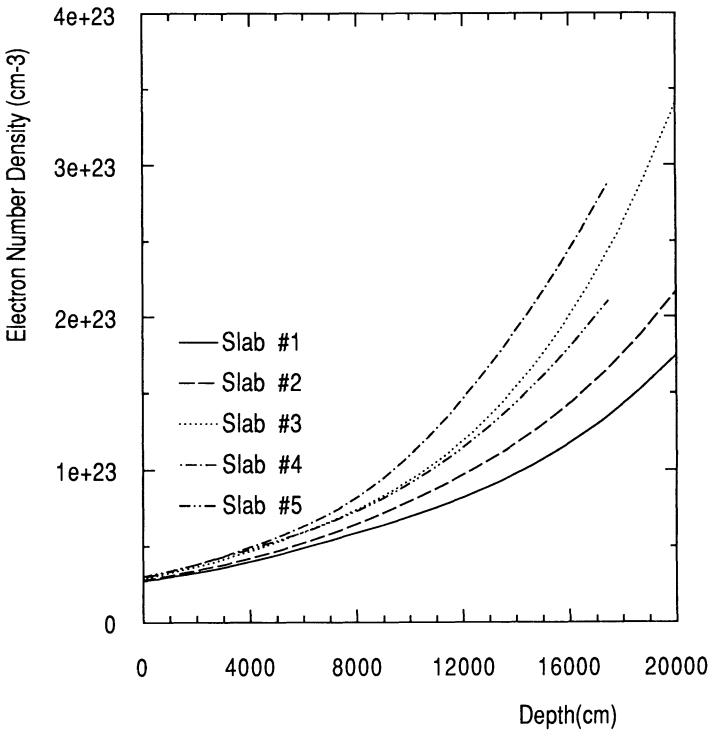

FIG. 6.—Electron number density as a function of distance into the one-dimensional slabs used in this paper.

III. PATCH MODEL ATMOSPHERES

To solve for the emitted radiation from the model slabs, we employ the combined Moment-Feautrier transfer solution technique described in our previous papers (Burnard, Klein, and Arons 1988, 1990). This technique allows us to solve for the transfer of radiation through a strongly magnetized Comptonizing plasma for arbitrary orientations of the magnetic field with respect to the local material.

We do not attempt to solve the detailed transfer problem for the cyclotron line, but instead remove a region surrounding the cyclotron line from the continuum and replace it with a net contribution of Comptonized line photons to the neighboring continuum. The extent of this region is determined, as in BKA, by the effective cyclotron line width multiplier, χ_s, defined in Arons, Klein, and Lea (1987). Thus, the radiation in the continuum is not strongly dependent on the exact frequency of the cyclotron resonance, and the small variations of B with distance into the slab can be safely neglected.

A key feature of this solution technique is that it allows for a abitrary magnetic field orientation and the accompanying requirement for increased angular resolution, while still efficiently treating density and temperature inhomogeneity in the slab material. As described in BKA, the combined Moment-Feautrier technique has substantial computational advantages over the direct Feautrier technique employed in other studies (Mészáros and Nagel 1985*a*, *b*), due to the way in which the

TABLE 2

SUMMARY OF MODEL SLAB CONDITIONS

Slab	Depth	τ_{sc}	τ_{th}	$N_{e,S}$	$N_{e,D}$	$T_{e,S}$	$T_{e,D}$	B	Θ_B
1.....	20000	6110	13	2.67E+22	1.74E+23	7.36	11.85	44	0°0
2.....	20000	7375	20	2.74E+22	2.16E+23	7.45	12.59	44	13.7
3.....	20000	10470	25	2.84E+22	3.39E+23	7.59	14.25	44	22.9
4.....	17500	8506	15	2.90E+22	2.89E+23	7.68	13.75	44	27.2
5.....	17500	6505	16	2.98E+22	2.10E+23	7.80	12.70	44	90.0

NOTES.—This table summarizes the five slab models used here. The column headings are the slab number, the thickness of the slab in cm, the Thomson scattering optical depth of the slab, the Thomson thermalization depth (at a frequency 3 times the surface temperature) of the slab, the surface density, the density at depth, the surface temperature in keV, the temperature at depth in keV, the magnetic field strength in keV, and the local inclination of the magnetic field with the slab normal direction.

angular and frequency redistribution of the photons are computed in separate iterated steps. For the slabs presented here, where the number of angle points in 96, this computational advantage amounts to a reduction of 10^5 in computer time and 10^4 in memory relative to the direct Feautrier solution technique. Thus while solution of these slabs would be computationally prohibitive with the direct Feautrier technique, the combined Moment-Feautrier technique allows their solution in approximately one hour of Cray X/MP time per slab.

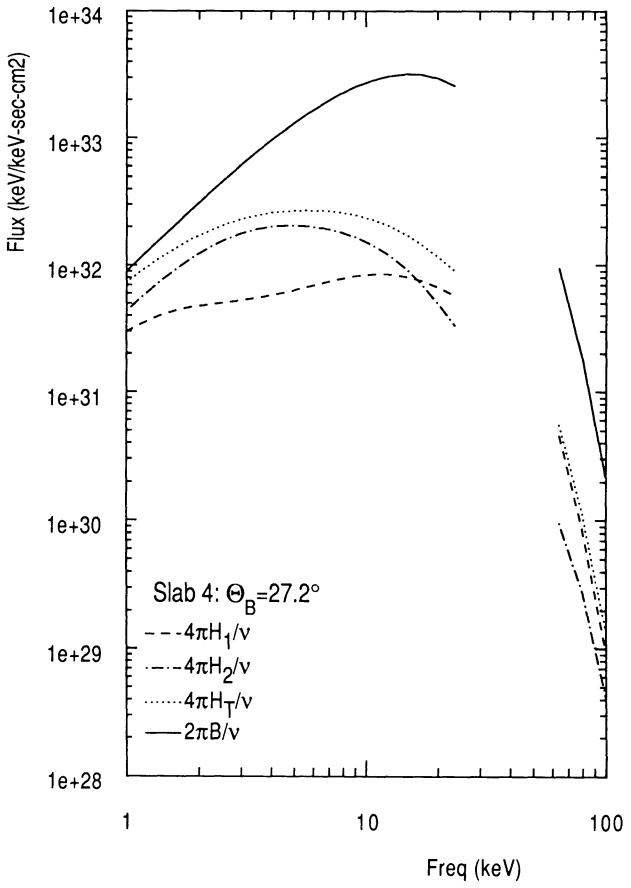

FIG. 8.—Emergent photon flux for slab 4, where the magnetic field direction is at an angle of $\Theta_B = 27°.2$ with respect to the slab normal. The flux in ordinary and extraordinary modes are shown with dashed and dash-dot lines, respectively. The dotted line represents the total flux. For comparison, the blackbody (Wien Law at the temperature of the slab surface) flux is denoted by the solid curve. The photon flux from slabs 1–3 is nearly indistinguishable from that of the slab.

a) Slab Spectra

The slab model which make up the mode accretion mound are similar to the slabs studied in BKA, both in physical conditions (the slabs in this paper are slightly hotter and denser, but are not as deep) and in the properties of their radiative output. As a result of this similarity, portions of the discussion from the previous paper are appropriate, and are reiterated, here. For a more detailed description of individual slab models, refer to BKA.

The emerging photon fluxes for two of the slabs are shown in Figures 8 and 9 (the spectra from slabs 1–3 are nearly identical to that from slab 4). The characteristic crossover of the energy

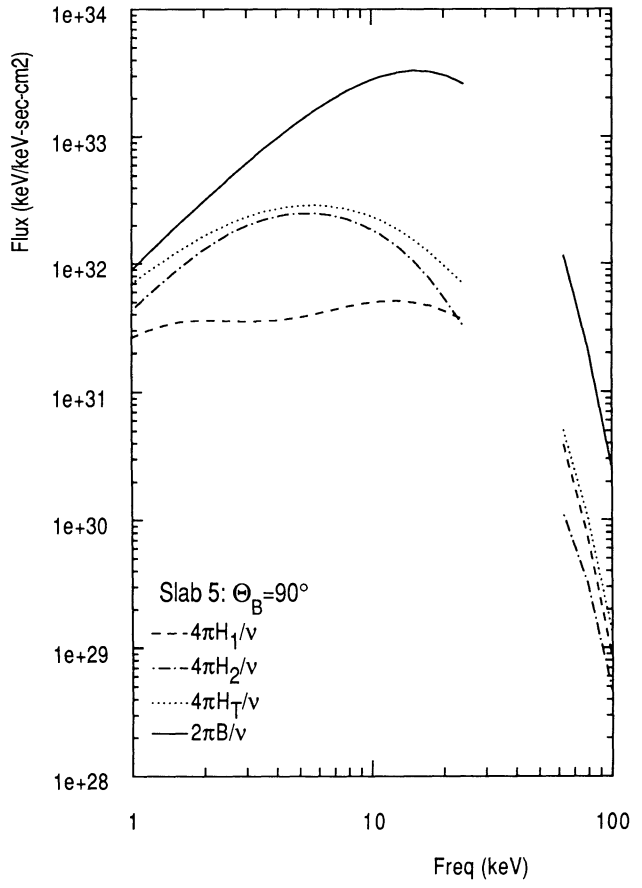

FIG. 9.—Emergent photon flux for slab 5, where the magnetic field direction is parallel to the surface of the slab, $\Theta_B = 90°$. The curves are labeled as in Fig. 8.

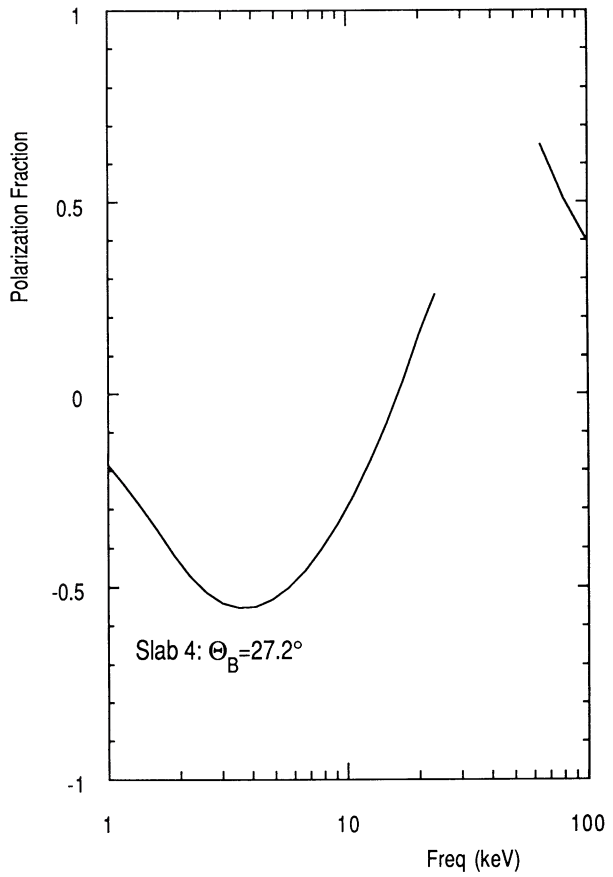

FIG. 10.—Polarization fraction, $[(H^1 - H^2)/(H^1 + H^2)]$, for slab 4, where the magnetic field direction is at an angle of $\Theta_B = 27.2$ with respect to the slab normal.

emitted in each of the polarization modes near 10 keV is present; this crossover shifts to slightly higher frequencies as Θ_B increases from 0° to 90°. The polarization fraction, $(H^1 - H^2)/(H^1 + H^2)$, for slab 4, which is similar to the BKA results, is shown in Figure 10.

To explain the general features of these spectra, consider an observer looking along the inhomogeneous slab's normal in the $\Theta_B = 90°$ model, i.e., perpendicular to the magnetic field, at frequencies well below the cyclotron frequency. In this orientation, all the photons entering the observer's line of sight scatter with the cross section for the ordinary mode ($\sigma^{1\to1}$) approximately equal to the Thomson cross section, while the cross sections for mode conversion and for direct scattering of the extraordinary mode ($\sigma^{1\to2}$ and $\sigma^{2\to2}$) are reduced below the Thomson value by a factor $(\nu/\nu_c)^2$ (Ventura 1979 or Arons, Klein, and Lea 1987, equation [B10]). Since the extraordinary mode photons escape more easily for *all* scatterings which send the photon toward the observer, one sees a relatively large enhancement of the extraordinary mode flux above the ordinary mode.

In the case where an observer looking along the slab normal also observes parallel to the magnetic field ($\Theta_B = 0°$), all the cross section are reduced by the same factor. Since the emergent flux includes contributions from directions not initially along the magnetic field, the net rate of photon loss in the ordinary mode is still smaller than the loss rate of extraordinary photons, but the difference is smaller than in the case where the observer looks across the magnetic field. Thus, at low frequencies, the polarization fraction should have a larger negative value for observation across the magnetic field than for observation along the magnetic field, as seen in our results. Above the frequency crossover, the situation is reversed due to the longer scattering cross section in the extraordinary mode, for frequencies in the vicinity of the cyclotron line. However, the difference between the mode intensities is not as great at these higher frequencies, because the cross sections are not so strongly angle dependent.

The spectra shown in Figures 8 and 9 resemble qualitatively the optically thick slabs studied in Mészáros and Nagel (1985*a*, *b*). In addition, if we were to show pulse light curves for the individual slabs, we could reproduce much of the complexity in rotation phase reported by these authors.

Looking ahead, one realizes, however, that the emission from the mound as a whole can be viewed as the superposition of the emission of a large number of slab models, all seen simultaneously at different orientations. Because the emission is from an optically thick medium, the properties of the radiation field (especially the polarization) observed at infinity depend both on the orientation of the magnetic field with respect to the observer *and* on the orientation of the magnetic field with respect to the slab normal, which controls the radiative proportions of the polarized intensities emerging from the slab. The angle between B and the observer's direction controls the relative magnitude of the scattering cross section as a photon undergoes its last scattering toward the observer. In an optically thin medium, this last scattering completely determines what the observer sees, independent of the orientation of the plasma with respect to the observer. In an optically thick medium, however, the relative proportion of the intensities in each normal mode which reach the surface of last scattering does depend on the orientation of the medium with respect to the magnetic field. As we shall see, this dependence on the orientation of the slabs tends to "wash out" any strong local features in favor of nonlocal features present over much of the surface of the mound. While the individual slab models have interesting variations due to the strong anisotropy in the cross sections, the radiation from the mound as a whole does not necessarily reflect this feature.

b) Modified Blackbody Model

As a comparison, and for use as a "quick and dirty" estimate of the emission from a given accretion mound, we have developed a modified blackbody model for the emission from a one-dimensional atmosphere, which gives an adequate representation of the computational results. The essential feature required is the inclusion of mode coupling between the polarization states. The details are presented elsewhere (Arons 1990, in preparation). Here we provide an outline of the technique and some typical results which are useful in understanding the numerical calculations.

The basic approach is to solve the transfer equations for diffusion of photons undergoing coherent scattering through a *homogeneous*, semi-infinite atmosphere. The form of the equations used is that of Arons, Klein, and Lea (1987), equation (39), except that coherent scattering in the cyclotron line replaces complete redistribution. The resulting coupled mode equations are equivalent to the diffusion equations used by Mészáros, Nagel, and Ventura (1980, hereafter MNV). The scattering cross sections for the continuum, including the mode-coupling cross section, and for the cyclotron line are

taken from Arons, Klein, and Lea (1987), while the bremsstrahlung opacity is taken from MNV, expression (1). We neglect nonorthogonality of the normal modes in the line—all coupling between resonant scattering in the extraordinary mode and line radiation in the ordinary mode is through the-scattering rate. We neglect Comptonization and the collisional emission of cyclotron photons. Finally, we assume that the density and temperature are homogeneous, since in coherent scattering, only the scattering optical depth is important. The assumptions of homogeneity and coherent scattering allow us to find an analytic solution of the transfer equations, of the same type as described in MNV.

We model atmospheric inhomogeneity by following the tactics lying behind the Eddington-Barbier relation of classical model atmosphere theory (Mihalas 1978). For unpolarized radiation in a homogeneous scattering atmosphere, it is known that the emergent intensity is

$$I_\nu \approx \epsilon_\nu B_\nu[T(\tau_\nu = \tfrac{2}{3})] ,$$

where $\epsilon_\nu \equiv [3\ \sigma_{abs}/(\sigma_{abs} + \sigma_{scat})]^{1/2}$ and $\tau_\nu \equiv n_e z[3\ \sigma_{abs}(\sigma_{abs} + \sigma_{scat})]^{1/2}$ is the thermalization optical depth from the atmosphere's surface down to physical depth z (Felten and Rees 1972). $\tau_\nu = \frac{2}{3}$ corresponds to the depth where the difference between the mean intensity and the Plank intensity is exp $(-\frac{2}{3})$.

The analogous rule for polarized radiation transfer, calculated in the diffusion approximation, is to find the Thomson optical depth $\tau_i(\nu)$ such that for mode i, the mean intensity satisfies

$$\frac{B_\nu\{T[\tau_i(\nu)]\} - J_\nu^{(i)}[\tau_i(\nu)]}{B_\nu\{T[\tau_i(\nu)]\}} = \exp\left(-\frac{2}{3}\right). \quad (3)$$

The mean intensity $J_\nu^{(i)}$ is found from the homogeneous radiative transfer solution, using the temperature and density corresponding to the initially unknown optical depth τ_i. This rule defines two thermalization optical depths, one of the O-mode ($i = 1$) and one for the X-mode ($i = 2$), at which the intensity in each mode is thermalized. Both the density and the temperature are needed to determine these optical depths, since the mean intensity $J_\nu^{(i)}$ depends on both quantities. Finally, because of two normal modes are coupled together, the solution of equation (3) depends on both intensities. In general, there is no simple analytic solution, although several useful approximations can be found depending on the strength of the mode coupling. Thus, the solution for the thermalization depth is found by iterative numerical solution of equation (3). Figure 11 shows the variation of the two thermalization optical depths with frequency, while Figures 12 and 13 show the density and temperature one thermalization depth into slab model 4.

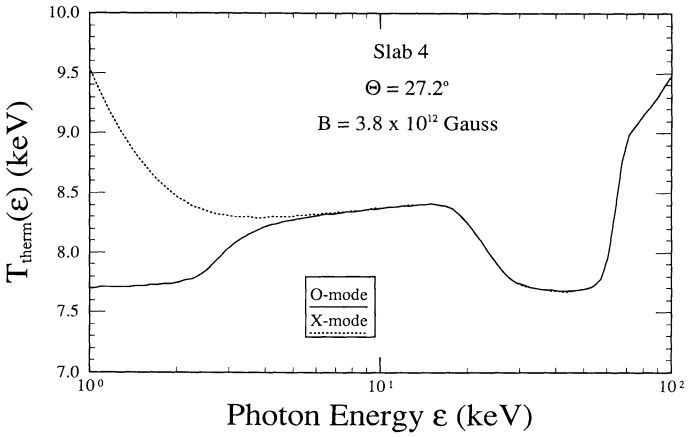

FIG. 12.—Electron temperature at a depth of one thermalization optical depth for slab 4.

The emergent intensity from this same slab, as calculated from the coherent scattering diffusion model, is shown in Figure 14. Comparison to Figure 8 shows that the diffusion model and the full numerical solution to the transfer equation agree quite well, with discrepancies not greater than a factor of 2. The major differences occur in the near vicinity of the cyclotron line, and at the higher photon energies. Here Comptonization and the addition of collisionally excited cyclotron photons, processes included in the numerical calculations but omitted in the diffusion model, act to flatten the spectrum. The fractional polarization of the diffusion model is shown in Figure 15. Comparison of this figure to Figure 10 shows that the diffusion model is a reasonable semi-quantitative means of estimating the spectropolarimetric output from optically thick accretion mounds.

The diffusion model also makes clear the reason for the lack of strong variation of the source function with optical depth. Figures 12 and 13 show that the thermalization density and temperature vary little throughout the 1–100 keV X-ray band,

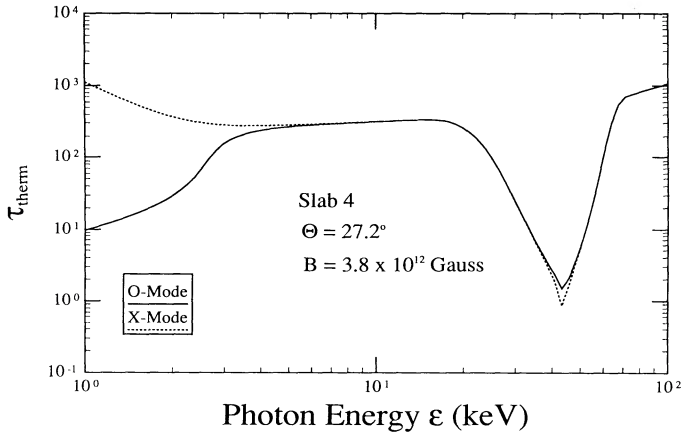

FIG. 11.—Depth into the slab 4 corresponding to one thermalization optical depth.

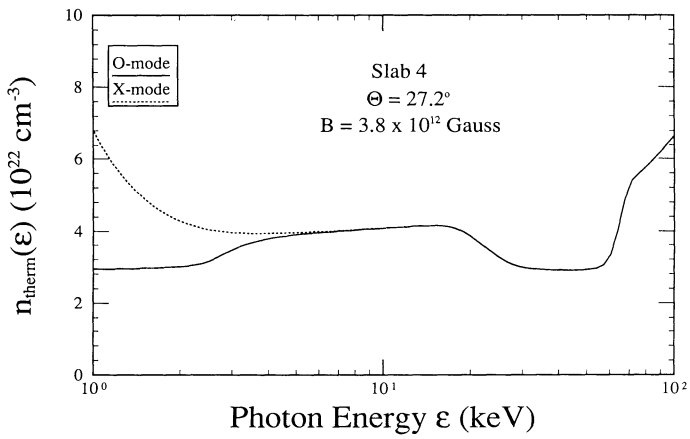

FIG. 13.—Electron number density at a depth of one thermalization optical depth for slab 4.

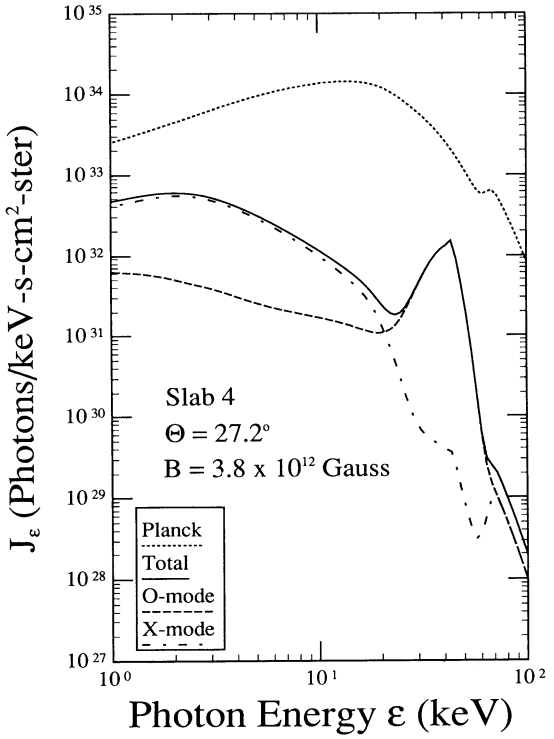

FIG. 14.—Photon intensity for slab 4 from the mode-coupled modified blackbody solution. Contrast this with the results from the Moment-Feautrier calculation show in Fig. 8.

for models with gradient scale lengths comparable to $\theta_c R_*$, as is the case in the model examined here. Thus, the spectrum differs little from that of a single-temperature modified blackbody.

The spectral behavior of such a modified blackbody at low energy can be understood by the following simple argument. As is clear from Figure 11, the *X*-and *O*-modes are uncoupled at low frequency, because the mode-coupling opacity $\propto \nu^2$ becomes small compared to the absorption opacity $\propto \sigma_s^{(i)} \sigma_{\rm brems}$ (MNV), where $\sigma_{\rm brems}$ is the bremsstrahlung opacity in an unmagnetized medium. In this uncoupled frequency regime, the emergent intensity is simply

$$J_\nu \approx \sqrt{\frac{3\,\sigma_{\rm abs}^{(i)}}{\sigma_s^{(i)}}}\,B_\nu \approx \sqrt{3\,\sigma_{\rm brems}\,\sigma_T}\,B_\nu\,,$$

as if the magnetic field were not present. This yields $J_\nu \propto \nu^1$ at low frequency, for a uniform-temperature slab. Because the temperature at the thermalization depth is close to being independent of frequency, the low-frequency behavior of our numerical and of our diffusion calculations is close to the uniform slab behavior. Only in a situation with much steeper gradients, leading to a substantial increase of the temperature at the thermalization depth with decreasing frequency, would one find a spectrum much flatter than ν^1.

This coupled-mode model has been developed here as a means of understanding the numerical calculations of a mound exposed to dark sky. As explained in § I, we believe a more realistic model should incorporate the effects of scattering in the radiative shock and possibly in the preshock accretion flow overlying the mound, in order to develop a fully realistic model. These overlying scattering layers partially insulate the mound, with some photons random walking back into the mound's surface. The effect increases the mean intensity at the mound surface over what one finds if the mound is exposed to vacuum. One can readily show that if the scattering in the overlying layers is modeled as photon diffusion in a *static* scattering medium, the coupled-mode model for the mound can be redone by requiring continuity of the mean intensity and the flux at the boundary between the mound and the overlying layer. The main difference is that the emergent intensity at the mound surface becomes $\sim \epsilon_\nu \max(1, \tau_{\rm layer}) B_\nu$ at low frequency, for example. There are no simple results at present for the modifications required by the motion of the medium, but since the infall speed is no more than mildly relativistic, we do not expect the amount of backscatter to be enhanced by more than a factor of 2 above what is found in a static model. Clearly, scattering models to include the effects of compression and shear in a moving medium will be useful.

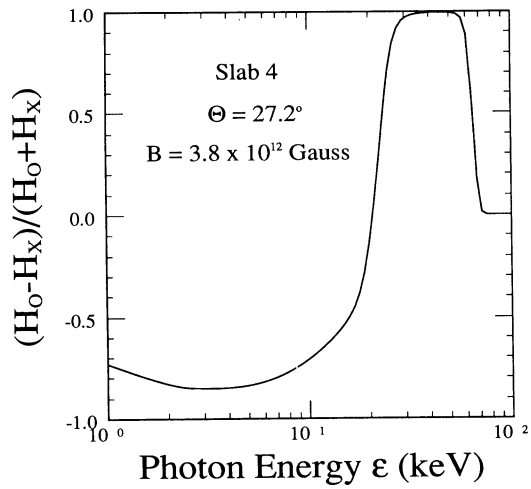

FIG. 15.—Polarization fraction for slab 4 from the mode-coupled modified blackbody solution. Contrast this with the results from the Moment-Feautrier calculation shown in Fig. 10.

IV. SYNTHETIC SPECTRA FROM THE ACCRETION MOUND

Once we have computed the angle-resolved emission from slab models representing the patches on the surface of the accretion mound, we can combine these results to form the emission from the whole mound. We can compute both total luminosity and net polarization data, as well as emission in a specific direction relative to the rotation axis of the neutron star, taking into account the inclination of the polar cap with respect to the rotation axis of the neutron star. We summarize the geometric transformations necessary to convert the local mound coordinates to those of a distant observer in the Appendix.

In computing the luminosity and polarimetry of these models, we have assumed that the magnetic field of the neutron star is dipolar and that the magnetic moment is centered on the neutron star, so that another identical polar cap is located in the opposite hemisphere. We further assume that the accretion flux is evenly distributed between the two polar caps. The basic symmetry of this configuration is reflected in the shape of the pulse profiles where both polar caps are visible. We discuss departures from the results presented here, due to an unaligned or nondipolar magnetic field geometry or an unequal accretion flux between the poles in § V.

a) Total Luminosity

We compute the total radiation emitted from the neutron star due to accretion on the polar caps in the following manner. We first compute the radiation emitted from each of the slab models, integrating over all angles and frequencies. Multiplying these slab emissivities by the required area for each slab to compose the accretion mound yields the total energy production of the mound. For the accretion mound studied here, the total luminosity in the range 1–100 keV is $L_x = 5.1 \times 10^{36}$ ergs s^{-1}, or 2.05×10^{44} photons s^{-1}.

Note that this corresponds to about 17% of the accretion luminosity L_c. This figure is consistent with the dynamical model described in § II, which predicted a mound luminosity substantially less than L_c, but still greater than $(H_s/R_*)L_c \approx 0.06L_c$.

b) Phase-Resolved Observable Data

In order to compute the phase-resolved spectra and polarimetry seen by an observer, we must take into account the orientations of the neutron star rotation and magnetic axes as well as the geometry of the polar cap itself. The orientation of the neutron star's rotation and magnetic axes, shown in Figures 2 and 3, strongly affect the characteristics of the observable data. These geometrical properties are not well-known, or only weakly constrained by existing data. Therefore we present results for several combinations of these parameters in order to demonstrate the variety of observable data that can be generated from a single polar cap model combined with various viewing geometries. We do not include general-relativistic effects in our calculations of the light curves, since our primary goal is to contrast the effects of the full mound geometry to the light curves produced by flat polar caps, and this can be done with simpler Newtonian calculations.

To produce phase-resolved data, we must compute the local orientation of the line of sight of an observer for each of the slab models comprising the surface of the accretion mound (see the Appendix). Once this computation has been made, we can simply sum over the contributions of each of the slabs (weighted by their respective areas). The phase-resolved data are then a series of calculations based on the lines of sight that occur as the neutron star rotates with respect to the observer.

We present results for three polar cap inclinations and three observer inclinations with respect to the rotation axis of the neutron star. These angles are, for the polar cap angle, 15°, 45°, and 75°, and, for the observers position, 10°, 40°, and 80°. A few simple rules aid in explaining the results. First, if the sum of these two angles is less than 90°, then only one of the polar caps is ever visible to the observer. In this case, the pole will be viewed from an angle between $|\Theta_{cap} - \Theta_{obs}|$ and $|\Theta_{cap} + \Theta_{obs}|$. If however, the angles sum to greater than 90°, then both poles are visible—the "northern" pole being visible at rotation phases near 0 and ± 1, while the "southern" pole would be visible near phase ± 0.5. Figure 16 illustrates, for several viewing geometries, how the observer's view of the neutron star and its polar caps varies as the star rotates.

i) *Flat Polar Cap Model*

To attempt to illustrate the observable differences between our self-consistent mound model and that of a simple flat polar cap model, we have produced light curves and spectra for a polar cap consisting only of a single-slab model (our slab 1) lying flat on the surface of the star. The flat polar cap model has been adjusted to have the same total area as the mond model. We present flat cap model data only for the viewing angles $\Theta_{cap} = 75°$ and $\Theta_{obs} = 40°$, which adequately illustrates the differences between flat and mounded emission regions.

Figure 17 shows the pulse light curves from visible from a flat polar cap model with viewing angles of $\Theta_{cap} = 75°$ and $\Theta_{obs} = 40°$. Notice that these light curves vary noticeably with frequency and are also quite strongly (>95%) pulsed. The strong pulsation is due to limb darkening—the fact that when the pole is near the limb of the star the cap is seen nearly edge-on.

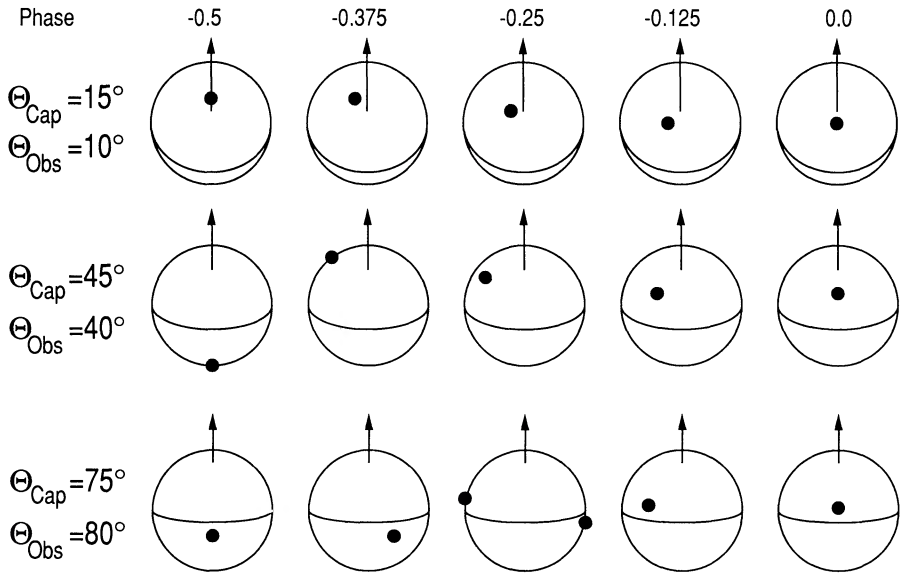

FIG. 16.—Observers view of the rotating neutron star and its polar caps as a function of rotation phase for three different sets of viewing angles. The viewing angles are $\Theta_{cap} = 15°$, $\Theta_{obs} = 10°$, in the upper panel; $\Theta_{cap} = 45°$, $\Theta_{obs} = 40°$, in the middle panel; and $\Theta_{cap} = 75°$, $\Theta_{obs} = 80°$ in the lower panel. The location of the polar caps are shown by solid black circles. Notice that in the upper panel only the "north pole" is ever visible to an observer, while in the middle and lower panels both poles are visible for some fraction of the rotation phase.

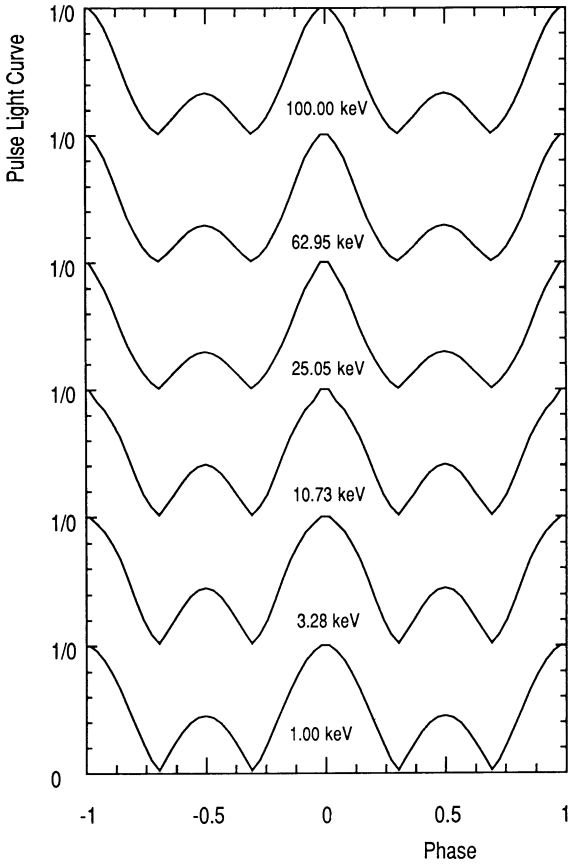

FIG. 17.—Pulse light curves from the flat polar cap model based on slab 1, for the viewing angles $\Theta_{cap} = 75°$, $\Theta_{obs} = 40°$. The observer's view of the star as a function of phase is similar to that shown in lower panel of Fig. 16.

The photon flux from the flat polar cap model is shown in Figure 18. Notice that the shape of the spectrum varies weakly with rotation phase, and that the amplitude of the spectrum varies strongly due to limb darkening.

ii) *Full Mound Model*

The particular polar cap model used here was chosen to match the gross features (total luminosity, polar cap area, and magnetic field strength) of the Her X-1 system. However, qualitative features in the Her X-1 data, such as the phase reversal between 1 and 6 keV or the asymmetry of the main pulse, indicate that the accretion mound is probably more complex than the particular mound geometry studied here. One product of our simple geometry is the small variation in temperature over the surface of the mound ($\sim 5\%$), and the relatively small difference between the temperature at the surface and at one thermalization depth into the mound ($\sim 15\%$).

One direct consequence of this uniformity is that the shapes of the pulse profiles are only weakly dependent on the photon frequency (while the overall amplitude of the pulsed intensity does vary strongly with frequency, as can be seen from the spectra). Since the total luminosity is the sum of the emissivity over the surface of the mound, spectral features present in single-slab models tend to be washed out unless they are present over a wide range of viewing angles. In other words, the apparent uniformity of the observed spectral output is due as much to the variety of angles at which different portions of the mound are viewed as it is to the uniformity of the mound model itself. Hence, for a nearly uniform mound, the shape of the light curves is dominated by the limb-darkening produced by the rotation of the neutron star, rather than the beaming pattern or shape of the spectrum of any particular region of the polar cap.

Figure 19 shows the light curves that would be observed for the nine possible combinations of polar cap and observer angles. As we pointed out earlier, there is very little variation in the profiles with frequency, so we present only the data for 7.7 keV, which fall within the range of most observations. This result can be contrasted with the light curves from the flat polar cap model, which vary more noticeably with frequency and are more strongly pulsed (see Fig. 17). That the mound model is less strongly pulsed (80% vs. $>95\%$) is due to the fact that, even when the pole is near the limb of the star, much of the surface of the mound is seen face-on.

Note that the light curves are fairly smooth due to the lack of steep gradients in the radiating material and the effect of averaging the emissivity over much of the mound surface. What is clearly visible, however, are the two distinct pulse components arising from whether one or both of the caps is seen by the observer.

Thus one possible interpretation for an object exhibiting sinusodial pulse profiles (no obvious candidates) is that only one polar cap is in view, while for objects with an "interpulse" (e.g., Cen X-3, 4U1538 – 52) both caps are seen as the neutron star rotates. Unfortunately such a simple categorization cannot be applied to many of the known sources due to the

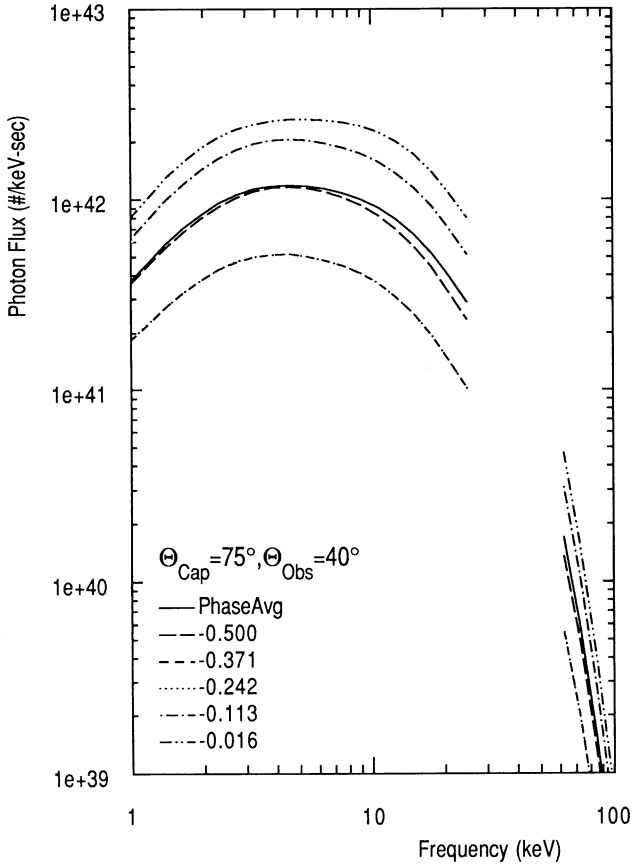

FIG. 18.—Phase-resolved spectra from the flat polar cap model based on slab 1, for the viewing angles $\Theta_{cap} = 75°$, $\Theta_{obs} = 40°$.

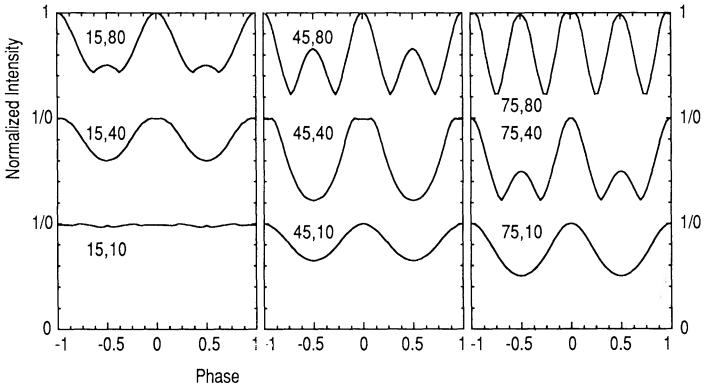

FIG. 19.—Pulse light curves from the full-mound model at a frequency of 7.7 keV. The left panel depicts models where $\Theta_{cap} = 45°$, and the right panel shows $\Theta_{cap} = 75°$

complexity of their pulse profiles and the inadequacy of a nearly uniform model in representing the actual accretion mound.

Figures 20–23 show the phase-resolved and phase-averaged spectra for our model polar cap for four characteristic viewing geometries. (The observer's view of the star at the rotation phases shown in these figures can be seen in Fig. 16.) The phase-dependent spectral data can be divided into two categories depending on whether one or both poles are visible to the observer. In the case where one pole is visible, the phase-averaged spectrum closely matches the phase -0.25 data, where the star has rotated one-quarter turn from where the pole directly faces the observer (the upper panel of Fig. 16). In the case where the observer views both poles as the star rotates, phase -0.25 is near where the polar caps appear on the limb of the star (the lower panel of Fig. 16), and thus the limb-darkening effect is at a maximum. In this case, the phase-averaged spectrum is a more complex function of the viewing angles, since these angles also determine the fraction of the rotation phase that each pole is visible.

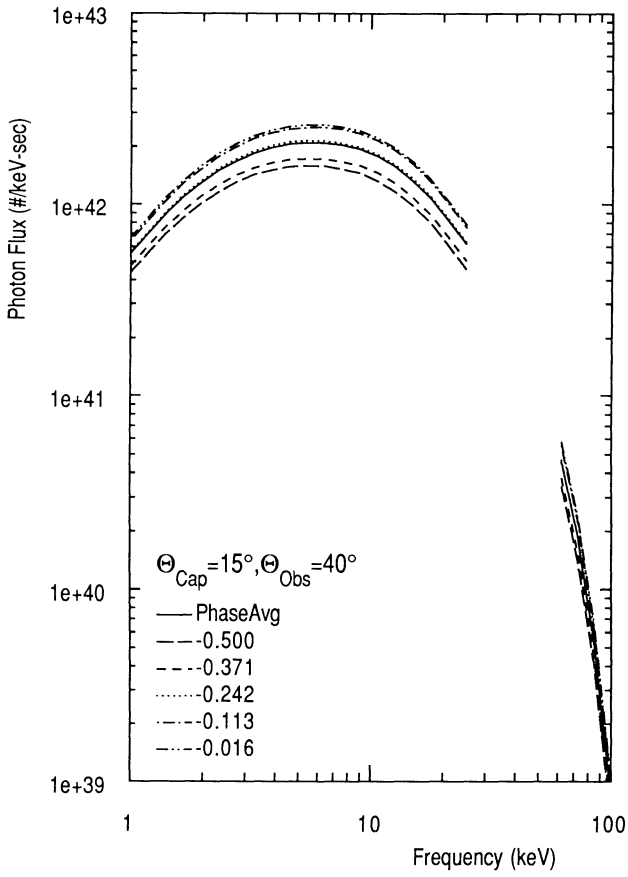

FIG. 20.—Phase-resolved photon spectra from the full-mound model for the viewing angles $\Theta_{cap} = 15°$, $\Theta_{obs} = 40°$. The observer's view of the star at the phase points shown is similar to the upper panel of Fig. 16. The solid line representing the phase-averaged data partially obscures the data from phase -0.242.

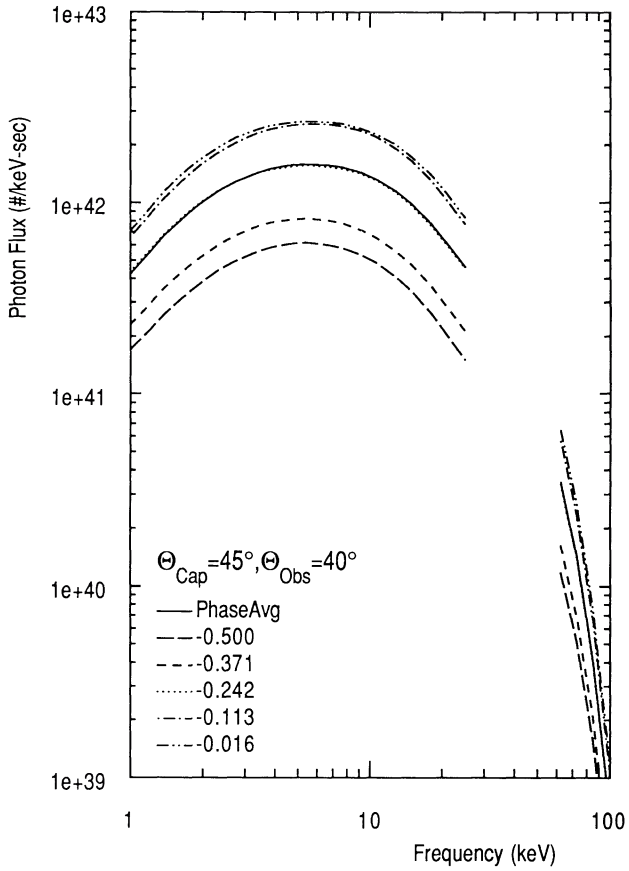

FIG. 21.—Phase-resolved photon spectra from the full-mound model for the viewing angles $\Theta_{cap} = 45°$, $\Theta_{obs} = 40°$. The observer's view of the star at the phase points shown can be seen in the middle panel of Fig. 16. The solid line representing the phase-averaged data almost completely obscures the data from phase -0.242.

Each of the viewing angle combinations show measureable variation of the overall amplitude of the spectrum with phase, except for case $\Theta_{cap} = 15°$, $\Theta_{obs} = 10°$ (not shown) where the observer always views the polar cap with an inclination of 25° or less. However, the spectral variation with phase can be attributed almost entirely to the geometric effect of limb-darkening. Notice also the lack of any variation in the shape of the spectra with rotation phase. This is due to the fact that averaging over the curved surface of the mound washes out any features that might result from the varying lines of sight as the star rotates. A uniform-mound itself does not produce any strong spectral features. The photon flux in Figure 22 can be compared with that from the flat polar cap model for the same viewing geometry in Figure 18. Notice that the flat polar cap

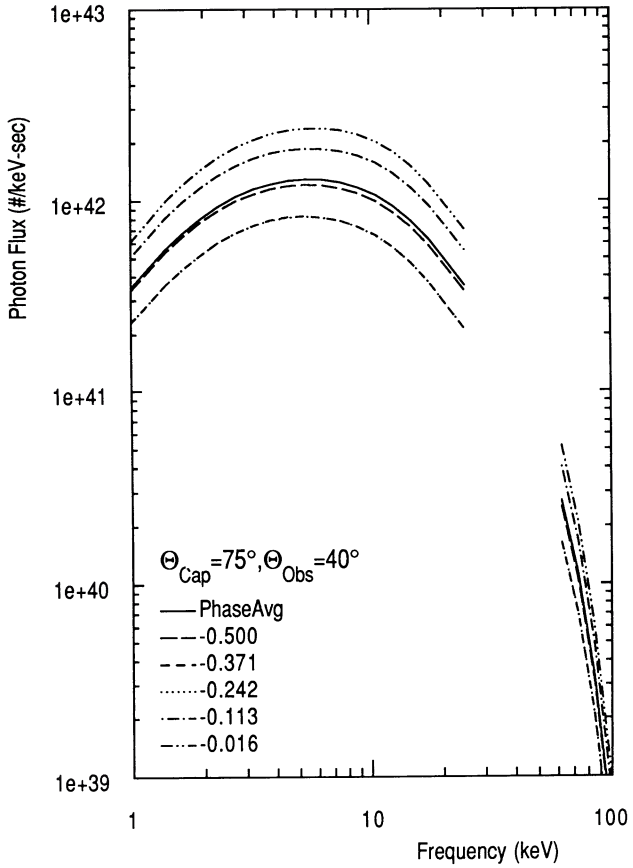

FIG. 22.—Phase-resolved photon spectra from the full-mound model for the viewing angles $\Theta_{cap} = 75°$, $\Theta_{obs} = 40°$. The observer's view of the star at the phase points shown is similar to the lower panel of Fig. 16.

spectrum has additional soft photon flux, and that the shape of the spectrum varies noticeably, although weakly, with frequency.

Figure 24 presents a summary of the phase-averaged polarimetry data, and indicates that our thermal mound has a recognizeable polarization signature. There is, however, little significant observable difference between the various geometries, except for the lower two curves, which represent models where one or both poles are viewed at large inclinations at all times. Limb-darkening in these cases causes a noticeable increase in the magnitude of the polarization fraction at frequencies below the cyclotron line.

When phase-resolved polarimetry data becomes available, this may provide an important probe of the emission region.

V. DISCUSSION

a) Comparison with Hercules X-1

The pulse light curve for Her X-1 is considerably more complex than the light curves produced by the model accretion mound studied here. Her X-1 exhibits a simple sinusoidal profile in the 0.5–0.8 keV band, while above 1.5 keV the profile reverses (90° out of phase with the low-frequency profile) and forms several distinct features (White *et al.* 1983). In order to begin to reproduce these features in our models, it will be necessary to introduce more complexity into either accretion flow, the magnetic field geometry, or both.

The spectra of Her X-1, and the majority of the known X-ray pulsars, are flatter at low energy than the spectrum obtained for the model presented here. Typically, the photon spectrum between 3 and 30 keV can be fit with a power law whose index is in the range 1.0–1.3. While it can be seen from Figures 8 and 9 that our model spectrum falls off less steeply than a single-temperature Wien spectrum, it is clear that the spectra from one of our slabs or from the mound as a whole cannot be represented by a single power law.

In this particular model mound, the temperature gradient between the surface and one thermalization optical depth at low frequency is insufficient to generate the observed soft-photon excess. It may also be necessary to consider additional alternatives for generating these "missing" photons, likely candidates include the two-photon double-Compton process studied by Kirk (1986), and the reprocessing of some of the photons from the mound by the surrounding region of the stellar surface.

b) Thin-Slab Models

In the past, attempts have been made to model the spectra from X-ray pulsars such as Her X-1 with a single backlit slab of optically thin material (Mészáros and Nagel 1985*a*, *b*), a model which might be geometrically interpreted as the emission from an atmosphere lying on the surface at a magnetic pole, rather than from the surface of a fully formed mound. They found that atmospheres with Thomson optical depths of ~4–8, backlit by a much lower temperature blackbody whose photon

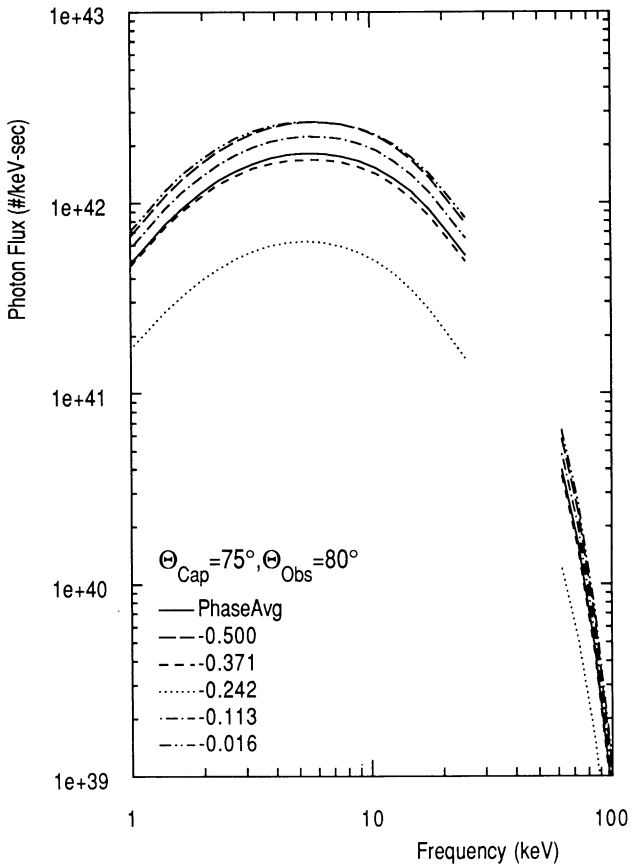

FIG. 23.—Phase-resolved photon spectra from the full-mound model for the viewing angles $\Theta_{cap} = 75°$, $\Theta_{obs} = 80°$. The observer's view of the star at the phase points shown can be seen in the lower panel of Fig. 16.

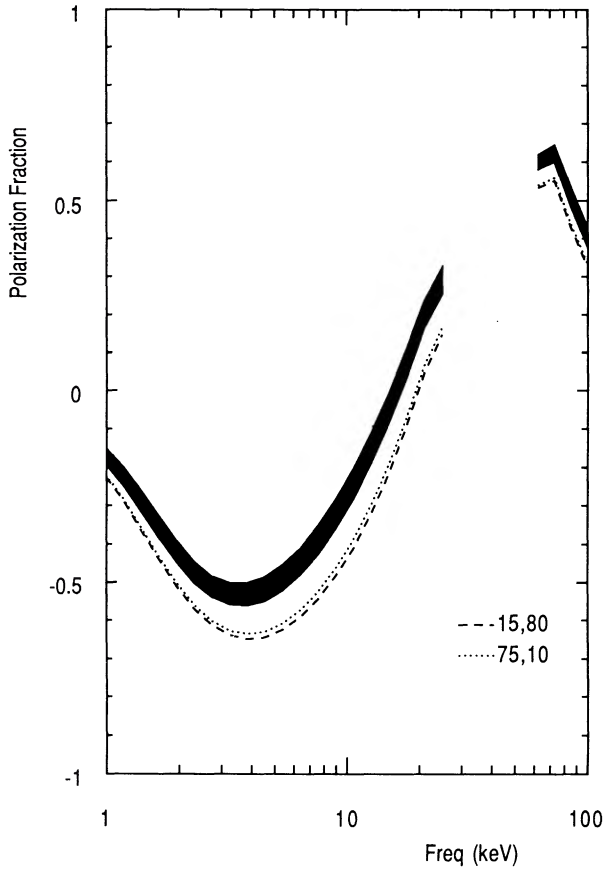

FIG. 24.—Phase-averaged polarization fraction from the full-mound model as a function of the viewing angles. All of the combinations studied here fall within the solid band, except for the curves labeled 15, 80 and 75, 10, which correspond to $\Theta_{cap} = 15°$, $\Theta_{obs} = 80°$ and $\Theta_{cap} = 75°$, $\Theta_{obs} = 10°$, respectively.

number was large compared to a real blackbody of the chosen temperature, led to rotation-averaged spectra not disimilar from the spectra of some of the accretion-powered pulsars. Our efforts differ in that we have attempted instead to model the emission from the mound itself, including the significant effect of the mound geometry on the observed spectra. In contrast to the static models of Mészáros and Nagel (1985*a*, *b*) the dynamically determined mounds considered here have Thomson depths on the order of 10^4–10^5. The spectrum produced by our mound model is significantly hotter than the 0.1 keV backlit assumed by Mészáros and Nagel (1985*a*, *b*) and is a significant fraction of the total luminosity of the star. However, the spectrum of the bare mound is not as good a representation of the data as the models of Mészáros and Nagel (1985*a*, *b*).

However, our model completely omits Comptonization by electrons in the high-velocity, radiatively mediated shock front between the mound and the freely falling column. The thickness of this shock corresponds to a Thomson optical depth of a few times (c/v_{ff}), roughly 6–9, essentially the same as found in the static models of Mészáros and Nagel (1985*a*, *b*). We suggest that *their* thin scattering slabs are a simplified representation of the Comptonizing shock front that appears in a real dynamical model. Such a shock is backlit by the photons from the mound, *with the fairly hot modified blackbody spectrum found here.* On the other hand, the shock is composed of very high velocity electrons, with energy/particle $\gg$ 10 keV, flowing in a semi-orderly manner along B, in contrast to the thermal plasma considered by Mészáros and Nagel (1985*a*, *b*). Clearly, there is a need for study of a physically correct model, in which the radiative *entropy* distribution generated by the mound has a form similar to the thermalized spectra found here, while the structure of the scattering atmosphere includes the large velocities, velocity gradients and spatial curvature appropriate to the accretion shock. It remains to be seen whether such a more reasonable model of the radiative shock, backlit by the type of mound model computed here, will reproduce the observed spectra.

c) Effects of Asymmetrical Magnetic Fields or Accretion Flows

We can qualitatively discuss the modifications to the data presented here that would result from a dipole field not centered on the center of the star, from nondipolar magnetic field geometry or an unequal accretion flux between the poles.

An offset dipole field geometry would be discernable if both of the poles are visible to the observer as the neutron star rotates. As discussed earlier, when both poles are visible, the pulse light curve is made up of two components. In the centered case, the components are symmetrical in rotation phase, whereas, if the poles are not exactly opposite each other on the stellar surface, the pulse component from the polar cap will be located midway between occurrences of the component from the other polar cap. This type of phenomenon, combined with unequal accretion onto the poles, has been shown to be useful in the interpretion of the light curve of the pulsed transient EXO 2030+375 (Parmar *et al.* 1989), for example.

The effects of a nondipolar field, or of unequal accretion onto the polar caps are more difficult to guess. At the extreme, nondipolear fields include those with strong magnetic anomalies on the surface, in addition to the dipole field, which could lead to multiple polar caps. Elsner and Lamb's (1976) proposed explanation of the complex light curve of Vela X-1 at low X-ray energies might require such complexity. In a different example, an axisymmetric quadrupole superposed on a dipole of comparable strength leads to two regions where the accretion flow reaches the surface. One is topologically equivalent to a polar cap of a simple dipole field. The other is shaped like a thin belt going around the star in the hemisphere opposite the simple pole (Barnard and Arons 1982). In general, both such regions would be visible to the observer, with a total intensity light curve similar to the output from a dipole model.

Beyond these possibilities, one must also consider the effects of a nonuniform accretion rate across a single polar cap, e.g., a hollow-cone geometry, or intermitent accretion.

VI. CONCLUSIONS

We have demonstrated the importance of including the geometry of the emission region in computing the radiation field seen by an observer. The simple mound structure studied here has the effect of washing out much of the strong angular variation found in single-slab models. Since our dynamical model of the accretion flow leads to moundlike structures in the accretion flow, single-slab models are inadequate for representing the emission region of all but the lowest luminosity X-ray pulsars. We have found that, if the emission were to come from an exposed settling mound alone, with the relatively shallow temperature gradients appearing in the laminar flow model used here, the resulting spectra and light curves would not have the forms observed in X-ray pulsars. More realistic models (Klein and Arons 1990, in preparation) show much steeper gradients, which may increase the number of

low-frequency photons emergent from the mound. The mound model does pass the test of supplying an adequate photon number, since it is sufficiently dense to have a fully thermalized radiation field in its interior.

However, modeling the full energetics of the emission requires inclusion of the photon recoil in the radiative shock on top of the mound, since the settling in a mound of height $H \ll R_*$ releases only a fraction H/R_* of the total accretion energy. The photon drag in the high-velocity flow of the shock and the cold accretion flow above and around the shock may lead to the formation of a final surface of emission with smaller area and a smaller range of angles than would be encountered if the mound were directly exposed to view. A simple estimate of such drag (Arons and Klein 1990, in preparation) leads to an effective area of emission $\sim \pi R_*^2 \theta_c^2 (v_{\rm ff}/c)$, when $L_c \gg L_{\rm ED}\theta_c \sim 10^{37}$ ergs s^{-1}, instead of the mound area $\sim 2\pi R_* \theta_c H_s$ appearing in the model studied here. For lower luminosities, drag is less important and the radiating area is approximately that of the mound, with additional energy added by the shock. The model used in this paper is in the boundary between these two regimes, so that the geometry of the emission region would be similar to the emitting area used here, even if the shock were included. In all circumstances, a self-consistent model of both the dynamics of the accretion flow as well as the radiation field is needed, even in the simplest flow geometries, in order to determine the radiating area and its orientation with respect to the magnetic field.

We found that it is possible to estimate the radiation from a magnetized slab with a simple mode-coupled modified blackbody approach. This calculation currently neglects incoherence effects, but can still be used as a rough indicator to explore, and possibly narrow, the wide range of mound conditions that might warrant further study with the more accurate, but more costly, combined Moment-Feautrier technique used in this paper. We also briefly discussed the modifications needed in order to apply the modified blackbody model to the more realistic problem of a mound with an overlying shock and shrouding preshock flow.

In comparing the power-law spectra of the known X-ray pulsars with the essentially thermal spectrum of our mound, we find that the Comptonization of the mound photons in the radiative shock must play an important role in determining the observed spectra of the polar cap. In addition, since our model fails to reproduce the observed soft-photon excess, we can eliminate inhomogeneous source functions in models with shallow gradients as the source of the soft photon excess. We conclude, then, that systems with steeper thermal gradients, such as edges or bubbles in the accretion mound (Klein and Arons 1987; Arons 1987; Arons 1988) and/or additional soft-photon sources (e.g., the two-photon double-Compton process) are also required to accurately model the emission from X-ray pulsars.

The research reported here was supported by grant 89-05 from the Institute of Geophysics and Planetary Physics at the Lawrence Livermore National Laboratory to the University of California at Berkeley. Our work was also supported by grant AST 86-15816 from the U.S. National Science Foundation to the University of California at Berkeley, and by the taxpayers of the State of California. Part of this work was performed under the auspices of the U.S. Department of Energy at the Lawrence Livermore National Laboratory under contract W-7405-Eng-48.

APPENDIX

COORDINATE TRANSFORMATIONS

We describe the coordinate transformations necessary to convert the observer's viewing angle from an absolute frame, corresponding to the rotation axis of the neutron star, to the local frame of one of the slab patches representing the surface of the accretion mound. For simplicity, we neglect the height of the mound in computing the orientation and visibility of the patch regions representing the surface. The only orientation where the approximation departs significantly from nature is where the accretion mound passes just beyond the limb of the star. In reality, the top of the mound may remain visible over the limb of the star for a short time after the base of the mound has been obscured.

Figure 2 illustrates the orientation of the polar cap and the observer's line of sight in the absolute frame, aligned with the rotation axis of the neutron star. In the absolute frame, we represent the line of sight of the observer $\boldsymbol{O}$, with the pair of angles $(\theta^a_{\rm obs}, \phi^a_{\rm obs})$ and the location of the polar cap as $(\theta^a_{\rm cap}, \phi^a_{\rm cap})$. The vector specifying the position of the observer in the absolute frame is then

$$\vec{\boldsymbol{O}}_a = \begin{bmatrix} \sin(\theta^a_{\rm obs})\cos(\phi^a_{\rm obs}) \\ \sin(\theta^a_{\rm obs})\sin(\phi^a_{\rm obs}) \\ \cos(\theta^a_{\rm obs}) \end{bmatrix}.$$

In order to transform the observer's viewing angle from absolute coordinates to the coordinates of the polar cap, we form the rotation matrix

$$\mathbf{M}_{a\to c} = \begin{bmatrix} \cos(\theta^a_{\rm cap})\cos(\phi^a_{\rm cap}) & \cos(\theta^a_{\rm cap})\sin(\phi^a_{\rm cap}) & -\sin(\theta^a_{\rm cap}) \\ -\sin(\phi^a_{\rm cap}) & \cos(\phi^a_{\rm cap}) & 0 \\ \sin(\theta^a_{\rm cap})\cos(\phi^a_{\rm cap}) & \sin(\theta^a_{\rm cap})\sin(\phi^a_{\rm cap}) & \cos(\theta^a_{\rm cap}) \end{bmatrix}.$$

In the polar cap coordinates, the observer's position is then given by

$$\boldsymbol{O}_c = \mathbf{M}_{a\to c} \cdot \boldsymbol{O}_a$$

and we can compute the individual observer angles from the x, y, and z projections of the vector $\boldsymbol{O}_c$

$$\theta^a_{\rm obs} = \arccos\left([\boldsymbol{O}_c]_Z\right)$$

$$\sin\left(\phi^c_{\rm obs}\right) = \frac{[\boldsymbol{O}_c]_X}{\sin\left(\theta^c_{\rm obs}\right)}$$

$$\cos\left(\phi^c_{\rm obs}\right) = \frac{[\boldsymbol{O}_c]_Y}{\sin\left(\theta^c_{\rm obs}\right)}$$

At this point we must determine which of the two polar caps is actually visible to the observer. The polar cap in the upper hemisphere (northern) is visible as long as $\theta^c_{\rm obs} < \pi/2$, otherwise the polar cap in the lower hemisphere (southern) is visible. If the southern polar cap is visible to the observer, then the observer's position vector must be adjusted to be relative to the southern polar cap as follows:

$$\theta^c_{\rm obs} = \pi - \theta^c_{\rm obs}$$

$$\phi^c_{\rm obs} = \begin{cases} -\pi + \phi^c_{\rm obs}\,, & \text{if } \phi^c_{\rm obs} > 0\,; \\ \pi + \phi^c_{\rm obs}\,, & \text{otherwise}\,. \end{cases}$$

If, in fact, the southern polar cap is visible, then we must recompute the observer's coordinate vector relative to the southern polar cap using the modified angles $\theta^c_{\rm obs}$ and $\phi^c_{\rm obs}$ from above

$$\boldsymbol{O}_c = \begin{bmatrix} \sin\left(\theta^a_{\rm obs}\right)\cos\left(\phi^a_{\rm obs}\right) \\ \sin\left(\theta^a_{\rm obs}\right)\sin\left(\phi^a_{\rm obs}\right) \\ \cos\left(\theta^a_{\rm obs}\right) \end{bmatrix}.$$

Figure 3 illustrates the relationship between polar cap coordinates and the patch coordinates appropriate to the surface of the mound. Notice that the angle θ^c_s represents the local inclination of the patch with respect to the polar cap, not its position, or altitude, as viewed from the stellar surface. The rotation matrix, which transforms from the coordinates of the polar cap to those of the local slab patch, is given by

$$\mathbf{M}_{c\to s} = \begin{bmatrix} \cos\left(\theta^c_s\right)\cos\left(\phi^c_s\right) & \cos\left(\theta^c_s\right)\sin\left(\phi^c_s\right) & -\sin\left(\theta^c_s\right) \\ -\sin\left(\phi^c_s\right) & \cos\left(\phi^c_s\right) & 0 \\ \sin\left(\theta^c_s\right)\cos\left(\phi^c_s\right) & \sin\left(\theta^c_s\right)\sin\left(\phi^c_s\right) & \cos\left(\theta^c_s\right) \end{bmatrix}.$$

In the coordinates of a slab patch, the observer's position is then given by

$$\boldsymbol{O}_s = \mathbf{M}_{c\to s} \cdot \boldsymbol{O}_c\,,$$

and we can compute the components of the observer's line of sight from the x, y, and z projections of the vector $\boldsymbol{O}_s$

$$\theta^s_{\rm obs} = \arccos\left([\boldsymbol{O}_s]_Z\right)$$

$$\sin\left(\phi^s_{\rm obs}\right) = \frac{[\boldsymbol{O}_s]_X}{\sin\left(\theta^s_{\rm obs}\right)}$$

$$\cos\left(\phi^s_{\rm obs}\right) = \frac{[\boldsymbol{O}_s]_Y}{\sin\left(\theta^s_{\rm obs}\right)}\,.$$

Finally, we must determine if this particular slab patch is oriented so as to be visible to the observer. An individual slab patch is visible if $\theta^s_{\rm obs} < \pi/2$, otherwise the patch lies on the opposite side of the mound and is not visible.

REFERENCES

Anderson, L. 1979, *Ap. J.*, **244**, 555.
Arons, J. 1988, in *Proc. Workshop on Plasma Astrophysics*, ed. T. D. Guyenne (Paris: European Space Agency), p. 117.
———. 1987, in *IAU Symposium 125, The Origin and Evolution of Neutron Stars*, ed. D. K. Helfand and J. H. Huang (Dordrecht: Reidel), p. 207.
Arons, J., Klein, R. I., and Lea, S. M. 1987, *Ap. J.*, **312**, 666.
Arons, J., and Lea, S. M. 1980, *Ap. J.*, **235**, 1016.
Barnard, J., and Arons, J. 1982, *Ap. J.*, **302**, 120.
Basko, M. M., and Sunyaev, R. A. 1976, *M.N.R.A.S.*, **175**, 395.
Burnard, D. J., Klein, R. I., and Arons, J. 1988, *Ap. J.*, **324**, 1001.
———. 1990, *Ap. J.*, **349**, 262 (BKA).
Burnard, D. J., Lea, S. M., and Arons, J. 1983, *Ap. J.*, **266**, 215.
Elsner, R. F., and Lamb, F. K. 1976, *Nature*, **262**, 356.
Felten, J. E., and Rees, M. J. 1972, *Astr. Ap.*, **17**, 226.
Giacconi, R., Gursky, H., Kellogg, E., Schreier, E., and Tananbaum, H. 1971, *Ap. J. (Letters)*, **167**, L67.
Kirk, J. 1986, *Astr. Ap.*, **158**, 305.
Klein, R. I., and Arons, J. 1987, in *IAU Symposium 125, The Origin and Evolution of Neutron Stars*, ed. D. K. Helfand and J. H. Huang (Dordrecht: Reidel), p. 246.
———. 1990, in *Proc. 23rd ESLAB Symposium on Two Topics in X-Ray Astronomy*, ed. N. E. White and T. D. Guyenne, ESA SP-296 (Paris: European Space Agency), p. 87.
Leahy, D. A. 1990, *M.N.R.A.S.*, **242**, 188.
London, R. A., and Flannery, B. P. 1982, *Ap. J.*, **267**, 18.
Mészáros, P., and Nagel, W. 1985*a*, *Ap. J.*, **298**, 138.
———. 1985, *Ap. J.*, **298**, 147.
Mészáros, P., Nagel, W., and Ventura, J. 1980, *Ap. J.*, **238**, 1066 (MNV).
Mészáros, P., Novick, R., Chanan, G. A., Weisskopf, M. C., and Szertgyorgyi, A. 1988, *Ap. J.*, **324**, 1056.
Mihalas, D. 1978, in *Stellar Atmospheres* (2nd edition, Francisco: Freeman), p. 157.
Milgrom, M., and Salpeter, E. E. 1975, *Ap. J.*, **196**, 583.
Nagel, W. 1981, *Ap. J.*, **251**, 288.

Parmar, A. N., White, N. E., Stella, L., and Izzo, C. 1989, *Ap. J.*, **338**, 359.
Parmar, A. N., White, N. E., Stella, L., Izzo, C., and Ferri, P. 1989, *Ap. J.*, **338**, 373.
Trümper, J., *et al.* 1978, *Ap. J. (Letters)*, **219**, L105.
Ventura, J. 1979, *Phys. Rev. D*, **9**, 1684.
Wang, Y.-M., and Welter, G. 1981, *Astr. Ap.*, **102**, 97.
Wheaton, W. A., *et al.* 1979, *Nature*, **282**, 240.
White, N. E., Swank, J. H., and Holt, S. S. 1983, *Ap. J.*, **270**, 711.

JONATHAN ARONS: Astronomy Department, University of California, Berkeley, CA 94720
arons@astroplasma.berkeley,edu

DAVID J. BURNARD: Apple Computer, Inc., 20525 Mariani Avenue, Mail Stop 22-AE, Cupertino, CA 95014

RICHARD I. KLEIN: Lawrence Livermore National Laboratory, Mail Stop L-23, Livermore, CA 94550